ADVANCED MATERIALS INTERFACES
www.advmatinterfaces.de

The Formation of the Solid/Liquid Electrolyte Interphase (SLEI) on NASICON-Type Glass Ceramics and LiPON

*Martin R. Busche, Manuel Weiss, Thomas Leichtweiss, Carsten Fiedler, Thomas Drossel, Matthias Geiss, Achim Kronenberger, Dominik A. Weber, and Jürgen Janek**

Most electrochemical energy storages (battery cells) consist of solid electrodes separated by a liquid electrolyte. If electrode materials are—at least partially—soluble in the electrolyte, detrimental mass transport between both electrodes (electrode cross-talk) occurs. The shuttle mechanism in lithium–sulfur batteries and leaching of Mn in high voltage cathode materials are important examples. Implementing a solid electrolyte (SE) membrane between the electrodes is a comprehensible approach to suppress undesired mass transport but additional resistances arise due to charge transport across the SE and charge transfer through the solid/liquid electrolyte interfaces. The latter contribution is often overlooked as its determination is challenging; however, these interface properties are crucial for practical application. In previous work, a resistive solid/liquid electrolyte interphase "SLEI" has been found at the interface between the SE lithium aluminum germanium phosphate in contact with a liquid ether-based electrolyte. Here, the aim is deeper insight into this interphase formation, referring to a lithium-ion conducting glass ceramic (NASICON-type) and the commonly used thin-film ion conductor lithium phosphorous oxide nitride. The growth of the SLEI is monitored by a combination of electrochemical characterization, X-ray photoelectron spectroscopy, and time-of-flight secondary ion mass spectrometry.

1. Introduction

The vast majority of currently commercially available lithium-ion batteries (LIBs) and next generation systems such as Li–S_8 and Li–O_2 are based on liquid electrolytes (LEs) due to the high bulk conductivity and because LEs easily wet and fill the porous electrodes. These features enable fast bulk and interface kinetics of Li-ion exchange required for high rate capability. Otherwise, in any LE-based battery system, secondary reactions are taking place apart from the desired Li^+-ion exchange that can be detrimental for cycle life and rate capability. This is especially the case if active material dissolves and diffuses from the cathode to the anode, creating a chemical short circuit or cross-talk, most particularly known as the polysulfide shuttle effect taking place in LE-based lithium–sulfur secondary batteries (LSSB).[1–7] Shuttle and active mass migration effects occur as well in LIBs[8] and redox catalyzed Li–O_2 cells.[9,10] Recent investigations prove that the migration of electrolyte decomposition products in high-voltage LIBs leads to strong capacity fading.[8] Main approaches to cure the parasitic shuttle shown for—but not limited to—LLSBs are as follows: 1) in situ established solid electrolyte interphase (SEI) formed via reaction of lithium and electrolyte compounds or additives (e.g., $LiNO_3$)[11] or 2) ex situ formed passivation layer (artificial SEI), using purely ion-conducting polymers[12] or inorganic coatings[13,14] are applied for anode protection. 3) The polysulfide diffusion out of the cathode is delayed by a cathode nanoscale architecture or sealing measures.[2,15–19] 4) "Solidification" of the Li–S_8 cell exclusively using polymers[20–23] or solid electrolytes[24,25] (SEs) circumvents the dissolution of polysulfides but suffers from slow transport kinetics of Li-ions inside solid lithium-ion conductors and across the interfaces. Especially the low rate capability of such systems limits their practical application as it is—beyond the energy density—the second crucial LIB property to enable energy storage for the electrification.

Most recent approaches refer to hybrid cells (anode/LE_a/SE/LE_c/cathode), comprising an LE in contact to the electrodes and an SE as a lithium-ion-selective barrier. The SE is separating anolyte (LE_a) and catholyte (LE_c) to suppress the chemical short-circuit as well as to reduce the danger of dendrite growth and electronic short-circuit.[26–39] Hybrid cells can be tailored to 1) allow fast kinetics of the LE/porous electrode interfaces as well as 2) apply thin solid electrolyte membranes to limit the Li-ion path length through the solid phase with lower conductivity.

Dr. M. R. Busche, Dr. M. Weiss, C. Fiedler, T. Drossel, M. Geiss, Dr. A. Kronenberger, Dr. D. A. Weber, Prof. J. Janek
Institute of Physical Chemistry
Justus-Liebig-University Giessen
Heinrich-Buff-Ring 17, Giessen D-35392, Germany
E-mail: Juergen.Janek@phys.chemie.uni-giessen.de
Dr. M. Weiss, Dr. T. Leichtweiss, Dr. M. Geiss, Prof. J. Janek
Center for Materials Research (LaMa)
Justus-Liebig-University Giessen
Heinrich-Buff-Ring 16, Giessen D-35392, Germany
The ORCID identification number(s) for the author(s) of this article can be found under https://doi.org/10.1002/admi.202000380.

DOI: 10.1002/admi.202000380

As a unique advantage, both LEs can be optimized separately for the anode and the cathode. Few approaches on hybrid next generation cells have been published: films of Lithium-ion exchanged Nafion[26] (a sulfonated tetrafluoroethylene-based fluoropolymer-copolymer) or Nafion-coated polymeric separators[40] were used as Li-ion selective membranes. Recently, Zhang et al. reported on an Al_2O_3-coated polymeric separator[29] and Li et al. used V_2O_5 as a polysulfide barrier.[30] Vizintin et al. showed promising cycle life of a hybrid LSSB with an inorganic ceramic membrane.[32] The application of glass ceramics of the NASICON-type as membranes is increasingly studied over the last three years.[31–36,38,41–43] Most recently, our group presented a novel approach to improve redox mediated Li–O_2 cells with an ion-selective membrane.[44] Lately, also garnet-type LLZO was successfully applied as ion-selective membrane in Li–S and Li-ion batteries.[45,46] Regardless of the active material in the electrodes, an ion-selective membrane for any hybrid cell has to meet the following demands, addressing its contribution to cell resistance, lifetime, and weight. 1) Fast conduction of the mobile ions with a transference number t^+ approaching unity, 2) an adequate electrochemical stability window and 3) high chemical stability in the LE environment are imperatives. This includes the solvents, the conducting salts, and additives as well as the soluble reduction species of the active material or secondary products. Linked to the fact that the conductivity of SEs is only rarely reaching the conductivity of LEs[25,47,48] and that the membrane should add only minimum weight to the cell system to keep its energy density,[41] 4) the SE must not exceed thicknesses in the order of a few micrometers. 5) The membrane has to be dense and mechanically rigid to obtain a functional ion-selective barrier. To sum up, the ideal system will comprise a fast conducting, thin, and dense (electro-)chemically stable membrane.

In the hybrid cell setup, the implementation of a membrane obviously leads to two additional interfaces between the SE and the LE.[41] Across these interfaces, the ion-conduction mechanism changes from the diffusion of solvated ions in the LE to the hopping ion transport mechanism present in the solid.[41,44] For each of these transport processes, a contribution to the cell impedance and the respective activation energy can be assigned and measured.[49–56] Beyond this, at the very interface, desolvation of the ions takes place and the ions have to penetrate the SE, moving through the phase boundary as schematically depicted in **Figure 1**. Recently, we revealed the formation of a solid/liquid electrolyte interphase (SLEI) that arises when a solid ion conductor (LAGP, $Li_{1.3}Al_{0.3}Ge_{1.7}(PO_4)_3$, lithium aluminum germanium phosphate) is in contact to the most commonly used LE for LSSBs, LiTFSI (lithium (bis)trifluorosulfonylimide, $LiN(SO_2CF_3)_2$) in a binary solvent mixture of 1,3-dioxolane (DOL) and 1,2-dimethoxyethane (DME).[41] The SLEI grows within the first 100 h of contact and adds a resistance contribution of ≈100 Ω cm^2 when reaching steady state.[41] Water impurities in the LE aggravate the effect, but do not change the composition of the SLEI. Thus, it was concluded that water impurities are not the essential reason for SLEI formation. The phenomenon of SLEI growth was extensively studied by means of a DC polarization technique by Schleutker et al.[57] The authors identified analogous growth of an SLEI in carbonate-based LE (EC:DMC) with $LiPF_6$ as a conducting salt when combined with LLZTO garnet-type SE. A higher SLEI resistance in the presence of water was also observed in this study, being attributed to formation of highly reactive HF from reaction of $LiPF_6$ and water. Recently, the system with carbonate-based LE and $LiPF_6$ was also studied using surface analysis methods and electrochemical impedance spectroscopy (EIS) by Liu et al.[58] The authors found an interphase resistance closely matching that resulting from the DC polarization study,[57] which increases until about 150 h after contact of LE and SE. In addition, LiF, Li_2O, Li_2CO_3, and organic fragments were detected in the SLEI. Another study analyzed the applicability of LLZO separators in Li–S cells. While the authors found a self-inhibiting interphase containing polysulfide decomposition products to prevent further decomposition, its resistance was not studied.[46] Unfortunately but obviously, the resistance of the solid/liquid electrolyte (SE/LE) interface or interphase ("SLEI") does not diminish with the reduction of the SE thickness but may sensitively depend on the effective area and chemical properties of the interface.[41] Therefore, beyond the chemical composition of SE and LE, the morphological properties of the membrane as well as the wetting ability, conductivity, and viscosity of the LE have to be focused and optimized to find an ideal SE/LE combination to circumvent a possible showstopper for hybrid cell setups.

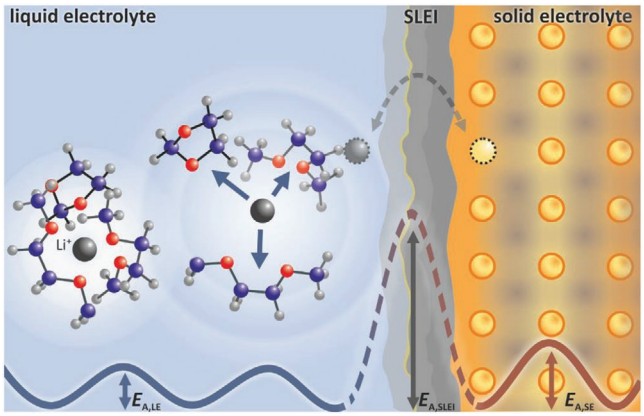

Figure 1. Schematic illustration of the ion transport through the phase boundary between an LE (with 1,3-dioxolane (1,3-DOL) and 1,2-dimethoxyethane (1,2-DME) as solvents) and an SE. Transition from the LE to the SE occurs via stripping off the solvate shell and transport across the heterogeneous phase boundary and interphase (solid/liquid electrolyte interphase, SLEI). As shown in a previous study,[41] contributions to the cell impedance and respective activation energies can be assigned to the conduction inside LE bulk, inside SE bulk (or intragrain and intergrain conduction for polycrystalline material), and transport across the phase boundary/interphase. The different contributions are distinguishable by means of the four-point impedance spectroscopy method and complementary reference measurements.

In this work, the SLEI is proven to also form on the most commonly used lithium-ion conducting glass ceramic LICGC and "LiPON" ($Li_xPO_yN_z$) as thin-film glass material with an ionic conductivity of up to 1.2×10^{-6} S cm^{-1}. The application of the thin-film SE is enabled by radio-frequency magnetron sputtering on porous alumina substrates as supporting spine, enabling contact of SE thin film and LE from both sides. The four-point measurement method introduced in ref. [41] is used to separately analyze the resistance contribution of the SLEI with special focus on the influence of the electrolyte solvents (single solvents DOL and DME and binary combination DOL/DME).

As the surface properties of these electrolytes are better controlled than for the LAGP samples, we aim at better-resolved depth profiling to unravel the structure of the SLEI by means of X-ray photoelectron spectrometry (XPS) and time-of-flight secondary ion mass spectrometry (ToF-SIMS). Omitting an in-depth study of the role of the chemical composition of the solid electrolyte, the impact of the interface topology is investigated by complementary atomic force microscopy (AFM) measurements. As a result, the impact of solvents, conducting salt as well as SE composition and morphology are evaluated and a schematic layer model of the SLEI composition is presented.

2. Results and Discussion

2.1. Basic Properties of the Solid Electrolytes

The structure of the LiPON SEs was evaluated by means of XRD and XPS. Figure S1 (Supporting Information) depicts the diffraction patterns of LiPON C1 and LiPON C2 reference samples providing evidence that the thin-film SEs are amorphous and not contaminated by crystalline phases. Thermal stability tests under He inert atmosphere reveal that the thin-films decompose to Li_3PO_4 above 200 °C as denoted in Figure S2 (Supporting Information). SEM micrographs (Figures S3 (C1) and S4 (C2), Supporting Information) denote a homogeneous coating of the porous alumina membranes and a smooth surface of the LiPON layer. However, considerable differences in the surface topology are made visible by means of AFM (Figure S5 and Table S1, Supporting Information): LiPON (C1) and LiPON (C2) sample surfaces possess mean roughness S_a values of about 250 and 490 nm, respectively. Thus, the effective area of the rougher LiPON (C2) samples is increased by a factor of 120%.

XPS analysis (see as well Section 2.3 and Figures S26 and S27 in the Supporting Information) of the thin films reveal an N/P ratio of about 1 for LIPON (C1 and C2). As published, the increase of ionic conductivity of amorphous LiPON compared to crystalline Li_3PO_4 is related to the substitution of oxygen atoms that are single or double coordinated by phosphorous atoms (P—O—P: bridging or P=O: nonbridging). The incorporation of nitrogen takes place as di- (—N=) or tricoordinated (—N<) by phosphorous and an increased N/P ratio results in a predominance of the dicoordinated species as extensively discussed in literature.[59,60] Most recently, Ceder, Dudney, and co-workers contradict to this widely accepted theory stating that nitrogen is not incorporated as tricoordinated species —N<.[61] However, an incorporation of bridging nitrogen anyway favors a decrease of the bridging oxygen/nonbridging oxygen ratio, induces disorder leading to percolation pathways, and results in lower uncompensated charge in the vicinity of the nitrogen, thus increasing the lithium mobility.[59,61] An N/P ratio close to unity as shown in our study is thus 1) showing a high level of incorporation of N into the structure and 2) causing Li^+ conductivity as confirmed by means of impedance analysis: as shown in the Supporting Information, we obtained room temperature conductivities of $(8 \pm 0.8) \times 10^{-7}$ S cm^{-1} and an activation energy of (521 ± 4) meV for LiPON C1 (Figure S6, Supporting Information) as well as $(1.1 \pm 0.1) \times 10^{-6}$ S cm^{-1} and (504 ± 2) meV (lateral) and (506 ± 2) meV (axial) for LiPON C2 (Figures S7 and S8, Supporting Information), respectively. Please note the very good agreement of lateral and axial measurements leading to the assumption that the lithium-ion transport in our LiPON films is isotropic. As sputter parameters had to be optimized with regards to comparably high thicknesses up to 5 µm and extremely low strain to the brittle porous substrates, the conductivities range a little under the maximum conductivity of 1.2×10^{-6} S cm^{-1} reported by Bates et al.[62,63] An overview of our parameter study that is added to the Supporting Information reveals that we had to sacrifice part of the ionic conductivity in favor of a higher growth rate (Figure S9, Supporting Information) and reduced strain on the brittle substrates. In line with the literature, the electronic partial conductivity is in the order of magnitude of 1×10^{-12} S cm^{-1} (C1) and 1×10^{-13} S cm^{-1} (C2), resulting in ionic transference numbers t^+ that deviate from unity after the 7th (C1) and 8th (C2) digits.

For the LICGC used as received from Ohara, Rietveld refinement reveals a main phase of $Li_{1+x+y}Al_x(Ge,Ti)_{2-x}P_{3-y}Si_yO_{12}$ with a NASICON-type structure and $AlPO_4$ (7.4 wt%) as a side phase (see Figure S13 and Tables S2 and S3 in the Supporting Information). This is well in line with the material datasheet presented online. The electrical properties as shown in Figure S14 (Supporting Information) are very close to the datasheet, featuring a room temperature conductivity of $(8.3 \pm 0.3) \times 10^{-5}$ S cm^{-1} and an activation energy of (312 ± 9) meV for the intragrain and (406 ± 6) meV for the intergrain conduction. However, as this material is a commercial product and has been analyzed in various studies,[64] we refrain from a deeper analysis.

2.2. Four-Point Impedance Results and Temporal Evolution of the SLEI

Figure 2 denotes the impedance spectra obtained at room temperature after 1 h (black), 24 h (green), 48 h (blue), 72 h (yellow), 96 h (red), 120 h (purple), and 144 h (dark gray) after assembly of the four-point cells for six different SE/LE combinations featuring LiPON (C1) and LICGC in combination with DOL, DME, and the binary mixture of DOL and DME. The equivalent circuits used for the fit routines are given as insets in Figure 2c,f. Beyond an ohmic resistance in the high frequency domain, we identify two suppressed semicircles as further contributions to the overall spectra for LiPON-based cells. The Nyquist representation of the impedance spectra allows for an unambiguous identification of the SLEI resistance contribution due to the special four-point setup: the lithium reference electrodes suppress the impedance response of the liquid-electrolyte/working-electrode interface as further explained in Figure S19 (Supporting Information) and the fraction of the LE and SE can be identified by the reference measurements. Thus, it is possible to assign the components of the impedance spectra as given in **Table 1**. As expected, the solvent has a strong impact on the bulk Li^+-ion conductivity of the LEs and the respective resistance contribution R_{LE} (1), ranging at (3.0 ± 0.1) mS cm^{-1} for DOL, (7.2 ± 0.1) mS cm^{-1} for the binary mixture, and (7.7 ± 0.3) mS cm^{-1} for DME, respectively. This is shown in all experiments presented herein with high reproducibility, visible by the standard deviation given. The suppressed semicircle (2) occurs from the ion conduction through the amorphous SE thin film, modeled by the equivalent circuit

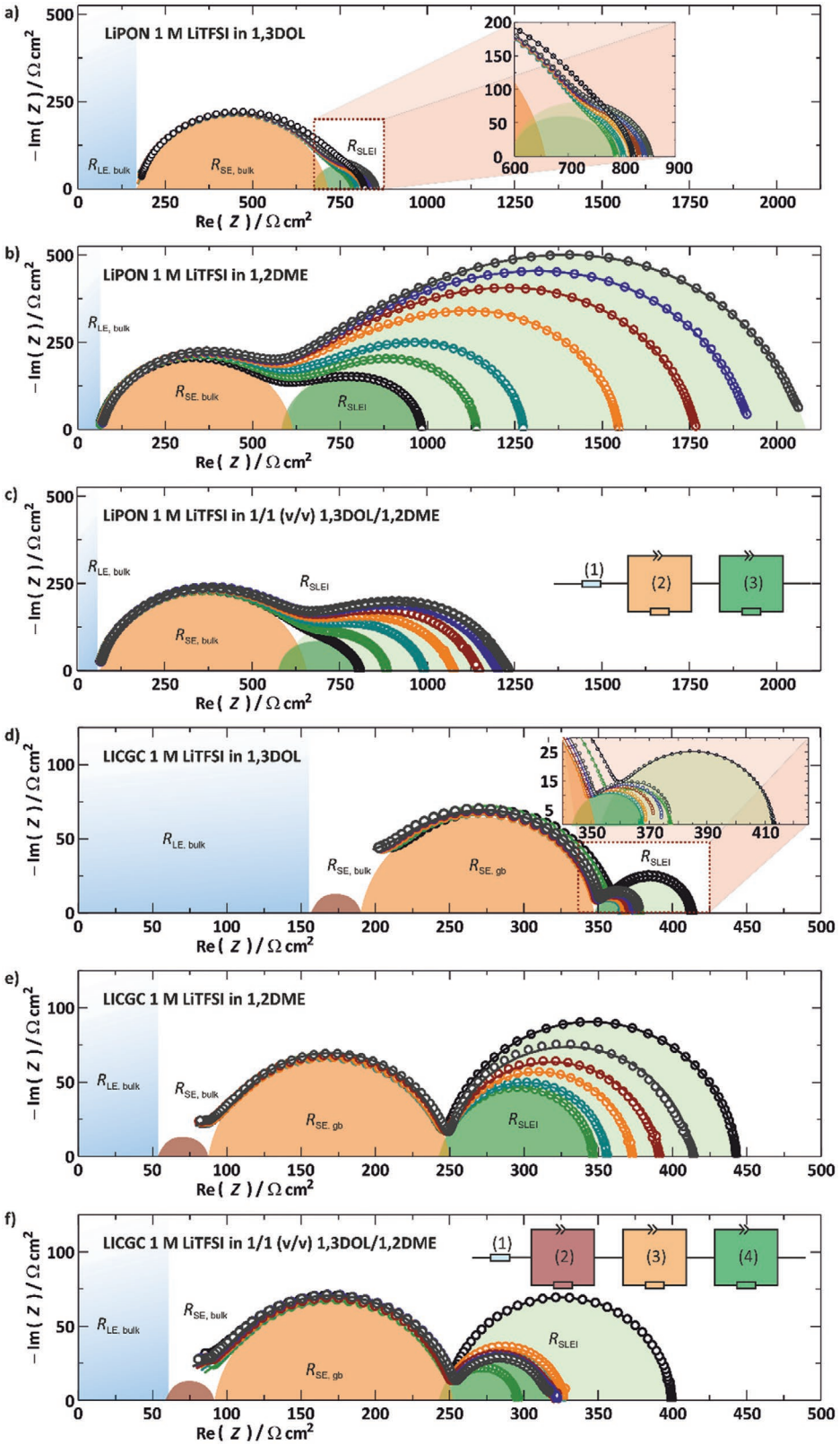

Figure 2. Impedance spectra of symmetrical four-point cells comprising LiPON (C1) a–c) and LICGC d–f) and the LEs 1 M LiTFSI in DOL a,d), DME b,e) and DOL/DME c,f). The Nyquist diagrams denote the temporal evolution of the solid/liquid electrolyte interphase (SLEI) after 1 h (black), 24 h (green), 48 h (blue), 72 h (yellow), 96 h (red), 120 h (purple), and 144 h (dark gray). The SLEI contribution is small for DOL, high for DME, and moderate for the binary mixture 1/1 (v/v) of DOL and DME. The raw data were fitted using the model circuits as shown in the insets.

Table 1. EIS fit results for the LIPON (C1)-based system.

Component/unit	Representation	DOL	DME	DOL/DME
$R_{LE,bulk}$ [Ω cm^2]	Ohmic resistance of the LE	165.5 ± 0.3	59.5 ± 0.9	68.5 ± 0.3
$R_{SE,bulk}$ [Ω cm^2]	Conduction in the amorphous SE	558.8 ± 1.8	546.0 ± 4.2	557 ± 2.1
$Q_{SE,bulk}$ [F s$-\alpha_{SE,bulk}$]		$(5.4 \pm 0.1) \times 10^{-8}$	$(5.7 \pm 0.5) \times 10^{-8}$	$(5.3 \pm 0.1) \times 10^{-8}$
$\alpha_{SE,bulk}$		0.825 ± 0.001	0.799 ± 0.005	0.831 ± 0.002
$C_{SE,bulk}$ [nF cm^{-2}]		5.1 ± 0.2	3.6 ± 0.7	5.5 ± 0.2
R_{SLEI} [Ω cm^2]	Transfer across the SLEI after 24 h/*after 144 h*	67.7 ± 1.9 *129.2 ± 1.5*	539 ± 3.8 *1511.7 ± 5.6*	261 ± 2.5 *621.8 ± 2.7*
Q_{SLEI} [F s$-\alpha_{SLEI}$]		$(5.9 \pm 0.5) \times 10^{-6}$ *$(6.4 \pm 0.3) \times 10^{-6}$*	$(3.9 \pm 0.1) \times 10^{-6}$ *$(3.3 \pm 0.1) \times 10^{-6}$*	$(5.4 \pm 0.2) \times 10^{-6}$ *$(6.5 \pm 0.1) \times 10^{-6}$*
α_{SLEI}		0.842 ± 0.014 *0.808 ± 0.007*	0.788 ± 0.005 *0.736 ± 0.007*	0.754 ± 0.006 *0.690 ± 0.003*
C_{SLEI} [μF cm^{-2}]		1.18 ± 0.29 *1.02 ± 0.13*	0.65 ± 0.06 *0.41 ± 0.04*	0.55 ± 0.06 *0.46 ± 0.03*

In order to ease comparison to the reference measurements, all resistance values are normalized to areal resistances. The values attributed to the SE are given as average values throughout the long-term measurements, and the values assigned to the SLEI are given after 24 h and after 144 h (italic), respectively. For details on the error propagation as well as on the calculation of capacitances on the basis of the Q and α values, we refer to the Supporting Information.

($R_{SE,bulk}Q_{SE,bulk}$). Please note both the excellent reproducibility of $R_{SE,bulk}$ with a relative standard deviation of just 2% and the good agreement with the reference measurement (Figure S6, Supporting Information), giving a value of (536 ± 10) Ω cm^2 when normalizing the lateral thin-film measurement by the ratio of the cell constants. This is also valid for the LICGC SE: here, we can deconvolve the impedance spectra of the SE by two suppressed semicircles, represented by the intragrain ($R_{SE,bulk}$, 2) and intergrain ($R_{SE,gb}$, 3) ion conduction within the polycrystalline SE. Unless the datapoints in the high-frequency domain are very scarce, not allowing for a correct deconvolution of the LE and the intragrain contributions, the reference measurement (Figure S14, Supporting Information) allows for a clear identification of the SE in the four-point spectra, featuring an overall resistance of (180 ± 3) Ω cm^2 and a high congruency of the frequency ranges.

Based on this discussion, the suppressed semicircle in the lowest frequency domain (3rd for LiPON and 4th for LICGC) is attributed to the SLEI as R_{SLEI}, showing extensive growth, whereas the other two contributions remain relatively constant throughout the long-term measurements of up to 165 h. Thus, as already published for LAGP[41] and LLZTO,[58] the evolution of the SLEI is as well shown for the SEs LiPON and LICGC. The resistance evolution can be divided into three periods: 1) immediately after contact of SE and LE (6–12 h), the resistance is slightly reduced for most of the LiPON samples. As all contributions are affected, we assume that a wetting or equilibration of the surface takes place. This is much more visible for the LICGC where all measurements show a significant reduction of R_{SLEI} within the first 24 h. We assume dissolution of surface residuals, comprising aliphatic carbons and Li_2CO_3 revealed by XPS reference spectra of the pristine samples (see Figure S28 in the Supporting Information). 2) Subsequently, the resistance monotonously rises, 3) at least tending to a stabilization phase as indicated by the decreasing slope and/or the constant R_{SLEI} reached eventually. Beyond this and as one major finding of this work, we point out that both the nominal value R_{SLEI} and its growth rate depend significantly on the solvent used as visible in the spectra (Figure 2) and the temporal evolutions of all resistance contributions of LE, SE, and SLEI (**Figure 3**).

This tendency is reproduced for all three SEs, but most clearly visible for LiPON (C1), presumably due to the very smooth surface and exclusion of any contamination by lab atmosphere. The measurement with DOL (Figures 2a and 3a) denotes a low R_{SLEI} of 68 Ω cm^2 after 24 h, growing by a factor of 190% in 144 h. The analogous experiment using DME as solvent results in a dramatically increased effect with R_{SLEI} growing from 539 Ω cm^2 after 24 h to 1511 Ω cm^2 at 144 h (Figures 2b and 3b). This represents an aggravation of R_{SLEI} by 1200% compared to DOL. The binary mixture shows a medium effect starting from 260 Ω cm^2 and stabilizing at 620 Ω cm^2, which is ≈2.4 times higher than after 24 h and 480% higher compared to the result with DOL, respectively. Based on that finding, we assume that—beyond the fact that in all cases presented herein an SLEI forms—DOL and DME contribute differently to the surface layer. The first is showing a smooth and rather slow resistance evolution, the latter leads to a comparably fast resistance increase, not reaching a limit after 165 h. The binary mixture shows intermediate behavior with a finite resistance contribution.

As the impedance spectra for LiPON (C1) allowed for more accurate fits than for polycrystalline samples like LICGC and LAGP, we could as well analyze the capacitances of the different SLEIs, derived as denoted in Figure S21 (Supporting Information): while the SLEI grown in DOL shows a significantly higher capacitance in the range of $C_{SLEI,\ DOL}$ = 1.1 μF cm^{-2}, those evidenced in DME and the binary mixture have lower capacitances of $C_{SLEI,\ DME}$ = 0.4 μF cm^{-2} and $C_{SLEI,\ DOLDME}$ = 0.5 μF cm^{-2}. Furthermore, we notice a temporal evolution of the capacitances: 1 h after start of the measurement, all capacities are in the range of 0.4 μF cm^{-2} (mixture) to 0.65 μF cm^{-2} (pure solvents). After 24 h, the value for DOL is significantly increased to (1.2 ± 0.3) μF cm^{-2}. While $C_{SLEI,\ DOLDME}$ grows as well during

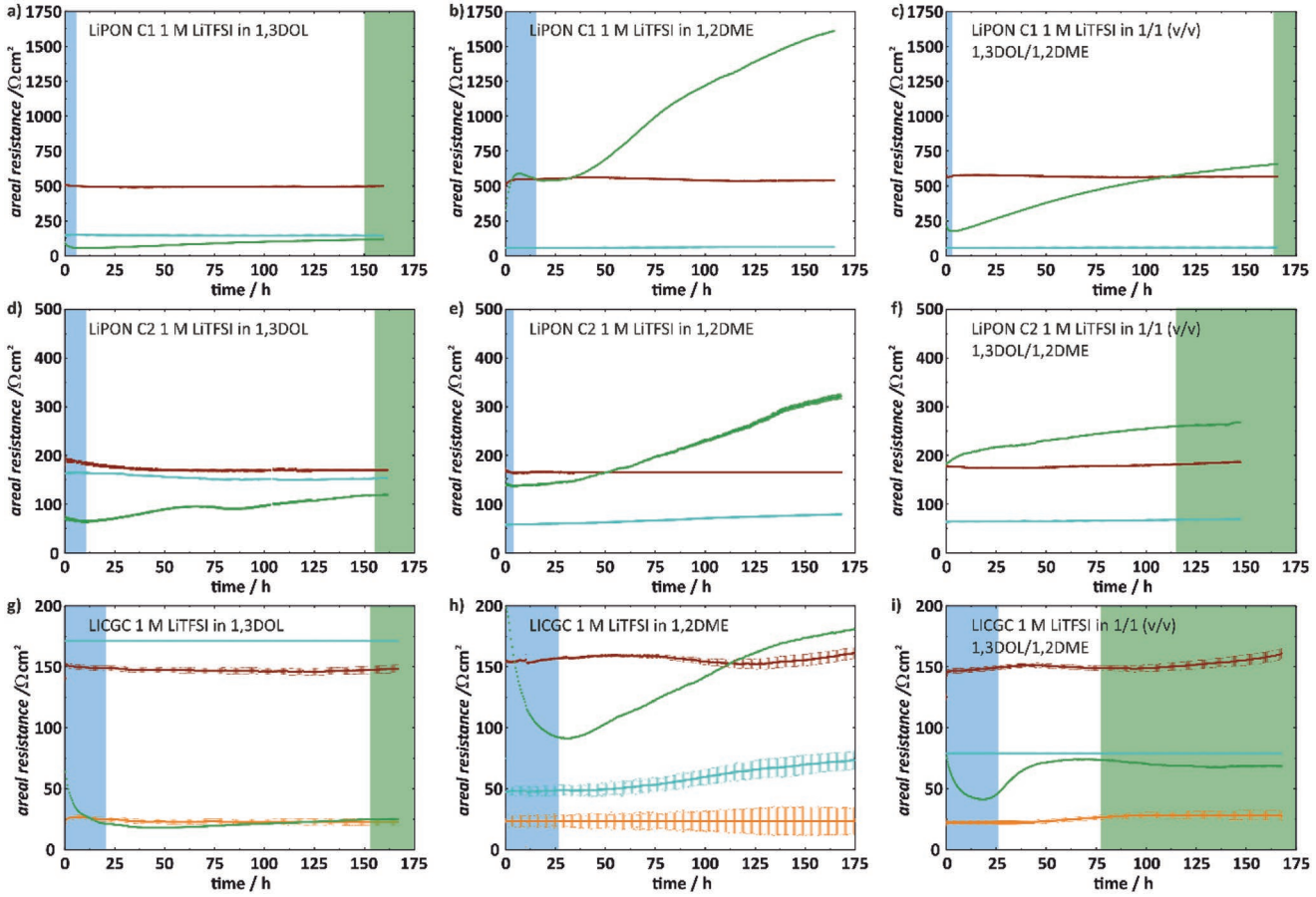

Figure 3. Comparison of the time dependence of the resistance contributions to the 4P spectra for LiPON C1 a–c), LiPON C2 d–f), and Ohara LiCGC for all LE systems 1 M LiTFSI in DOL (1st column), in DME (2nd column), and in DOLDME (3rd column): the LE (bulk, blue) and the SE contributions (LiPON bulk/LiCGC intragrain; red and LICGC intergrain; yellow) remain relatively constant, whereas the SLEI (green) shows significant time-dependent growth. As further explained in the text, the SLEI contribution is significantly dependent on the LE solvent. For each dataset, the resistances and respective errors were derived from data fitting, based on the $R(RQ)(RQ)$-equivalent circuit for LiPON samples and the $R(RQ)(RQ)(RQ)$-equivalent circuit for the LICGC samples.

the first 24 h, $C_{\mathrm{SLEI,\ DME}}$ remains stable in this period. After that, all SLEI capacities show a tendency to decrease to a stable value around 1.0 µF cm^{-2} for DOL and 0.4 and 0.45 µF cm^{-2} for DME and the binary mixture, respectively.

In order to shed more light on these phenomena, we performed further analysis on the impedance data for LiPON C1 using the distribution of relaxation times (DRT) method as presented in Figure S22 (Supporting Information). For all three experiments, we identify one process at $\omega = 340$ kHz with stable relaxation time during the long-term measurement, which can be attributed to charge transport through the LiPON thin film. We assign a second process with increasing relaxation time (decreasing frequency) to the charge transfer through the SLEI. Here, we face a slight frequency reduction from $\omega = 10$ kHz after 1 h to 7.8 kHz after 144 h for DOL. The relaxation time for the charge transfer process through the SLEI, $\tau = RC = 2\pi/\omega$, thus increases from 0.6 to 0.8 ms. For the analogous experiment with DME, the relaxation time is significantly higher: after 1 h, the relaxation time is 2.7 ms (2.3 kHz) and grows to 6.0 ms (1.1 kHz). Again, the binary mixture shows an intermediate behavior, ranging from 0.5 ms (13.9 kHz, 1 h) to 2.5 ms (2.5 kHz, 144 h).

We can conclude that the EIS analysis of the different SE and LE combinations indeed shows that DOL and DME contribute differently to the SLEI formation: obviously, 1,3-dioxolane leads to a relatively low resistance contribution of the SLEI with a substantially higher capacitance and thus a low relaxation time of the charge transfer. Meanwhile, 1,2-dimethoxyethane supports the formation of an SLEI with a 12 times higher ohmic resistance, low capacitance, and very high relaxation time. The binary mixture always shows an intermediate behavior, which we assign to a superposition of the two different effects. We may link the capacitance and relaxation behavior to spatial properties of the SLEI: in a very simplistic model of a capacitive layer, the capacitance is inversely proportional to the layer thickness. In that case, the SLEI formed in DOL may possess much lower thickness as those found for DME and the binary mixture, which may range in the same order of magnitude. Thus, the extremely sluggish transport through the SLEI formed in DME cannot be explained by the bare layer thickness. This will be addressed in the following section.

2.3. Surface and Depth Analysis—Discussion of the SLEI's Layer Structure

The ex situ analyses by means of XPS and ToF-SIMS focus on the results obtained with the LiPON (C1) samples, which have never been exposed to lab atmosphere. All survey spectra and detail spectra acquired for this study are presented in Figures S23–S31 (Supporting Information), including results for LiPON C2 and LICGC samples. XPS detail spectra of carbon (C 1s), sulfur (S 2p) and fluorine (F 1s) of the LiPON (C1) samples treated for 8 days in four-point cells in DOL a–c), DME d–f), and the binary mixture g–i) are depicted in **Figure 4**. The binding energies attributed to species based on literature screening as well as their assumed origin are summed up in **Table 2**.

The C 1s signal can be deconvolved into five lines, which are attributed to the following species: the strongest intensity in the C 1s signal for the sample treated in DOL/DME refers to a binding energy of 286.5 eV, assignable to $R_3CO–R$,[71,69] and 284.8 eV, attributed to alcoholates R_3COLi,[69,72,73] both degradation products of DOL and DME. Based on the findings of Fiedler et al., alkoxide salts or carboxylate salts of lithium are formed by solvent decomposition[65] and are also attributable to these lines. Due to the multitude of surface components, a clear differentiation of these organic lithium salts is not possible by XPS. Furthermore, the line at 284.8 eV is also visible in the reference samples and it might be as well related to aliphatic carbon $-(CH_2)-$ to some extent. The component present at 287.9 eV is not visible in the DME sample and is assigned to carbonyl or polymeric species $(CH_2CH_2OCH_2)_n$ originating from DOL decomposition.[69,65,70] We find carbonates and/or semicarbonates (CO_3^{2-}, 289.4 eV) as inorganic salt components on all samples. All these components are well known to build up the SEI on metallic lithium anodes.[11,69,65,74]

The additional line at 289.4 eV represents the $(-CF_3)-$ group in LiTFSI[66] and is visible on all samples, presumably originating either from conducting salt residuals or LiTFSI decomposition. For all SEs analyzed in this study, the highest contribution of organic lithium salts is found in the binary mixture, while it is rather low for the single solvents. The signal assigned to poly-DOL or carbonyl is also more intense for DOL/DME compared to sole DOL. Thus, we assume cross-effects

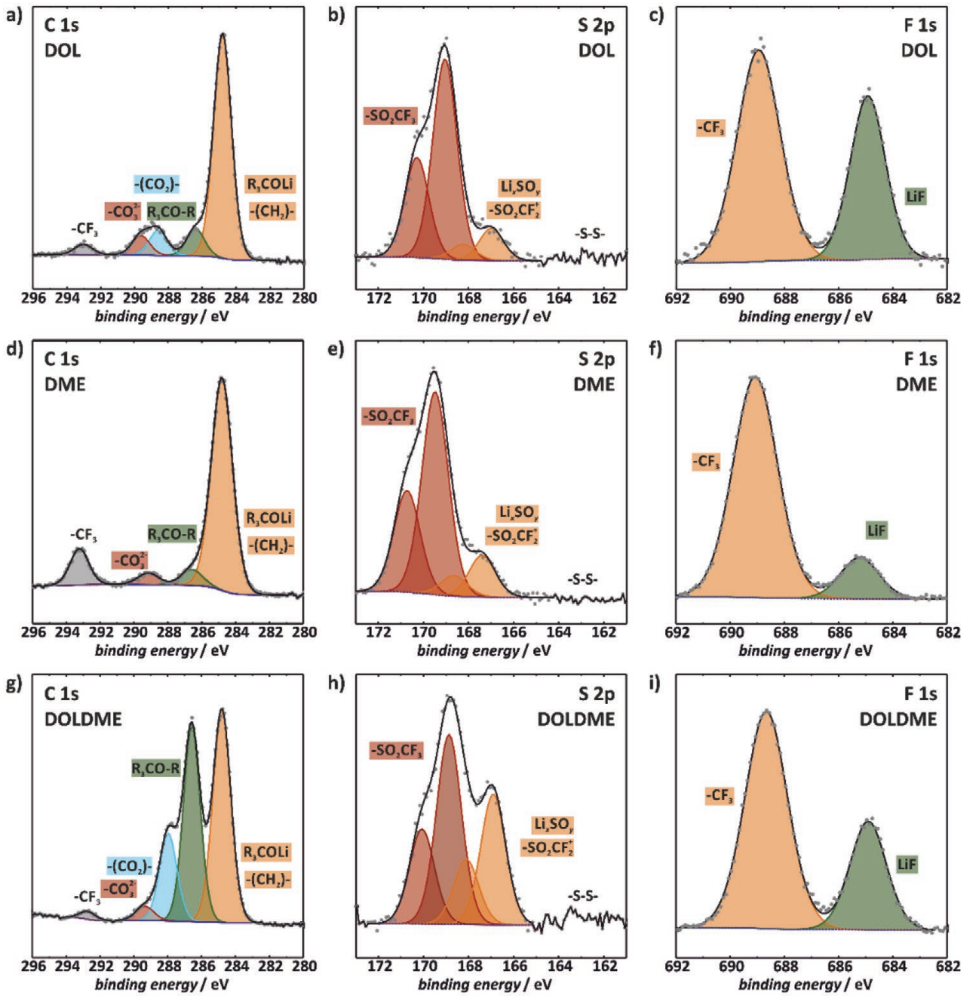

Figure 4. XPS detail spectra of carbon (C 1s), sulfur (S 2p), and fluorine (F 1s) for a LiPON (C1) sample treated for ≈160 h in 1 M LiTFSI in DOL a–c), DME d–f), and DOLDME g–i). For attributions of species to the binding energies refer to Table 2.

Table 2. Attribution of species to the binding energies observed via XPS.

Detail spectrum	Binding energy [eV]	Color	Attributed species	Ref.	Assumed origin
C 1s	292.8	Gray	$-CF_3$	[65,66]	LiTFSI conducting salt
	289.4	Red	CO_3^{2-}	[65,67,68]	Carbonates, e.g., Li_2CO_3 or semicarbonates (solvent decomposition products)
	287.9	Blue	$-(CO_2)-$ $(CH_2CH_2OCH_2O)_n$	[69,70] [65]	Carbonyl or polymeric species poly-DOL (DOL solvent decomposition products)
	286.5	Green	R_3CO-R C–O bond in RCH_2OLi or RCOOLi	[71,69] [65]	DOL/DME solvent residuals or decomposition products, alkoxides, or carboxylates
	284.8	Orange	R_3COLi $-(CH_2)-$C–C bond in RCH_2OLi or RCOOLi	[69,72,73] [65]	DOL/DME solvent residuals or decomposition products (alcoholates) aliphatic carbons, alkoxides or carboxylates
F 1s	688.6	Orange	$-CF_3$	[66]	LiTFSI conducting salt or LiTFSI decomposition product
	684.9	Green	LiF	[69,66]	LiTFSI decomposition product
S 2p	169.0	Red	$-SO_2CF_3$	[66]	LiTFSI conducting salt or LiTFSI decomposition product
	167.1	Green	$-SO_2CF_2^+$ or Li_xSO_y	[66,68] [69]	LiTFSI decomposition product
N 1s	399.5	Not shown	Imide groups	[66]	LiTFSI conducting salt or LiTFSI decomposition product
P 2p	133.6	Orange	PO_4	–	SE (LICGC)
	132.6	Orange	PON	–	SE (LiPON)

between the solvents, leading to the "fingerprint" of the SLEI in DOL/DME similar for LiPON, LICGC, and LAGP. The latter has been reported in our previous work[41] and confirmed by Manthiram and co-workers for the similar system.[39] Two different species can be identified in the S 2p spectra, which are attributed to sulfonyl groups–SO_2CF_3 from the conducting salt[66] or its decomposition products: referring to the signals at 167.1 eV, we assume that LiTFSI is decomposed as these are assigned to as sulfonyl residuals with stripped fluorine –$SO_2CF_2^+$ or Li_xSO_y.[69,66] This is as well supported by the F 1s spectra, confirming LiTFSI decomposition by identification of two representations of fluorine: one in LiF at 684.9 eV and one in CF_3 at 688.6 eV. On the pristine reference samples (Figures S26–S28, Supporting Information), no or only small fluorine and sulfur contaminations are detected. However, we denote a significant contamination by hydrocarbons and other carbon specimens for all samples and it is unclear if these residuals are fully removed during electrochemical treatment. Considering these limitations, we give the elemental quantification of the surface analysis as denoted in **Table 3** and Tables S5 and S6 (Supporting Information).

For all three SEs, treatment in the binary mixture leads to the highest amount of carbonaceous species on the sample surface, whereas the lithium content is the lowest. Furthermore, the phosphorous signal of the LiPON thin films as well as phosphorous, titanium, and germanium from the LICGC SE are suppressed most by the DOL/DME SLEI and the least by the DOL SLEI. At least from the XPS surface analysis, we cannot state that the SLEI with the strongest resistance impact, produced by the treatment in DME, shows a significantly higher thickness or compactness. The ambiguity of—especially the fluorine—species quantification, for instance visible in the comparison of LiF and CF_3 signals for the different LiPON samples (compare Figure 4 to Figure S30 in the Supporting Information) results in the necessity for complementary surface analysis. However, from the sole masking of the SE signals, we assume that the SLEI formed in DOL/DME is the thickest or most compact one, which is confirmed by XPS depth profiles denoted in Figure S32 (Supporting Information): a sputter time of approximately 1500 s is required to reach constant values for P 2p and very low values for C 1s. For those samples treated in the single solvent electrolytes, the SE is reached after max. ≈1000 s. Furthermore, the profiles hint at fluorine species accumulating inside the surface film, whereas carbonaceous and sulfuric species are located closer to the surface, especially for DME and DOL/DME. Due to the low depth resolution, the results obtained by XPS depth profiling are rather scarce. ToF-SIMS is used as a complementary method to the XPS measurements to i) support the differentiation of the SLEI components and ii) obtain more detailed information on the inner structure of the interphase. Depth profiles of LiPON samples treated for 8 days in the four-point cell obtained by ToF-SIMS and sputtering are denoted in **Figure 5**, comparing the results for electrolyte based on DOL (a), DME (b) and the binary mixture (c). For better legibility, we clustered the secondary ion signals into ions assigned to i) the SE and ii) the inorganic and iii) organic components of the SLEI. We chose a square-root-like scaling of the time axis in order to focus on the SLEI composition. The respective relative atomic masses of ion fragments denoted in the depth profiles

Table 3. Elemental quantification of a pristine LiPON sample and the SLEI on LiPON (C1) obtained by means of X-ray photoelectron spectroscopy and derived with relative sensitivity factors (RSFs) provided by the instrument manufacturer.

	O 1s	Li 1s	C 1s	P 2p	N 1s	S 2p	F 1s
				[at%]			
Reference	33.4	33.6	13.6	9.5	9.3	0.3	0.3
DOL	36.5	28.1	20.0	6.4	6.7	0.8	1.5
DME	32.0	22.2	34.1	4.3	4.1	2.4	0.9
DOL/DME	32.5	8.3	49.8	1.6	2.0	1.6	4.3

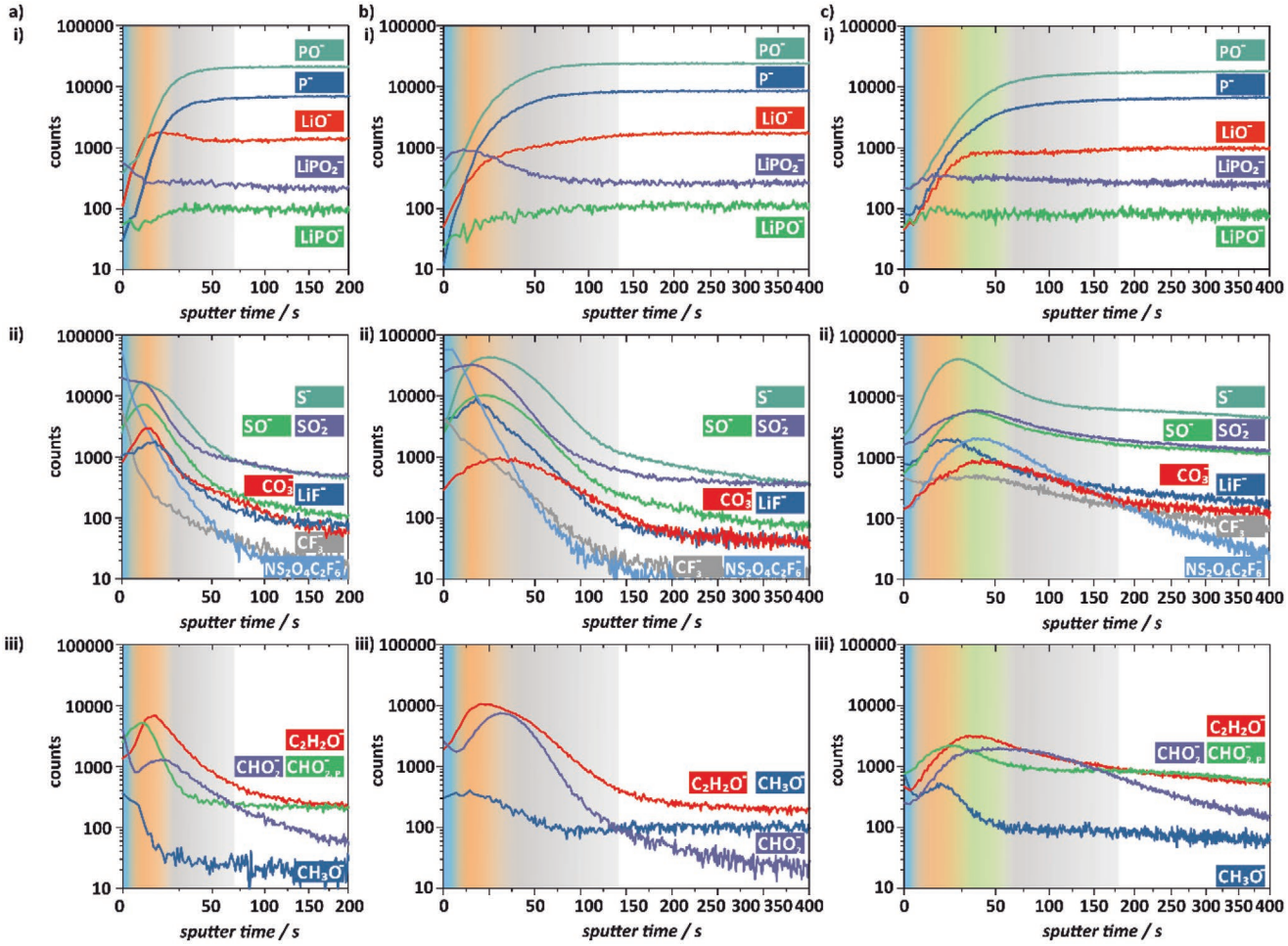

Figure 5. Comparison of depth profiling obtained by sputtering and ToF-SIMS analysis for LiPON (C1) samples treated for ≈160 h in 1 M LiTFSI in DOL a), DME b), and DOL/DME c). For each of the profiles, the selected secondary ion signals are assigned to SE fragments i), inorganic SLEI fragments ii), and organic LE fragments iii). Please note that only negative fragments are visible as analysis was carried out in negative ion mode to prevent information losses by detector saturation with Li^+. For assignment of the secondary ion masses/fragments to their respective origins refer to the discussion in the main text and Table S7 (Supporting Information).

are summarized in Table S7 (Supporting Information). Along with consecutive sputtering, the secondary ion signals change nonsimultaneously, hinting at an inhomogeneous film and allowing for the definition of different regions, which are color-coded for easy reference.

It is confirmed by the ToF-SIMS depth profiles that indeed the SLEI thickness or compactness rises in the order DOL < DME < DOL/DME: constant values for the PO^- and P^- signals are achieved after ≈70 s for DOL, ≈130 s for DME and ≈200 s for DOL/DME (Figure 5), pointing out that the solid electrolyte is reached. For the single solvent electrolytes, a first region (I, blue) is identified, where high amounts of LiTFSI fragments ($NS_2O_4C_2F_6^-$, CF_3^-, and SO_2^-) are detected as secondary ions, hinting at conducting salt residuals. This is not surprising as the SLEI surface was in direct contact to the liquid electrolyte before disassembly and washing. Interpreting the secondary ion signal assigned to CHO_2^-, we assume that carboxyle salts RCO_2Li (e.g., formate) are moderately enriched in this first region for DME and highly accumulated for DOL. A second region (II, red) is reached for both DOL and DME after approximately 4 s of sputter time. Beginning with SO_2^- (in region I), SO^- and S^- (in region II) are reached one after another with increasing sputter times. As all of these fragments originate from LiTFSI, we assume prudently that a high fragmentation of LiTFSI by the sputter beam may occur easier in deeper regions of the SLEI. This hints at a stronger degradation of the conducting salt inside the SLEI. For DME, the degradation of LiTFSI seems to be more prominent (see comparison in Figure S33 in the Supporting Information). The decomposition of $LiN(SO_2CF_3)$, involving the precipitation of LiF, Li_2S, and Li_3N, has already been published.[75,76] It has also been suggested that traces of acidic compounds present in the electrolyte (e.g., HF) react with Li_2CO_3, forming LiF and semicarbonates $-CO_3$, which then decompose.[77–79] In all solvents, we find carbonate $-CO_3^-$ fragments originating from the second region, however, the signal of $-CO_3^-$ fragments is significantly lower for the DME and DOL/DME samples. Therefore, we assume that the carbonate formation is more pronounced in DOL.

Most important, the signal attributed to LiF^- shows a sharp maximum and the signal intensity is almost one order of

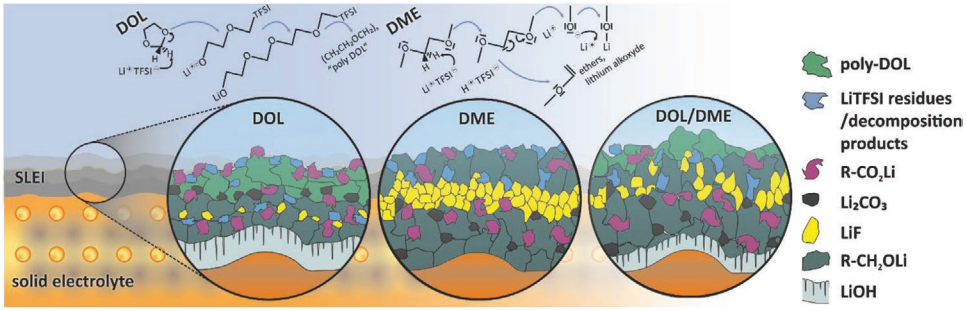

Figure 6. Schematic illustration of SLEIs formed in liquid electrolytes based on the pure solvents DOL and DME and their binary mixture, based on the depth profiles denoted in Figure 5 and the discussion in the main text. Assumed exemplary decomposition reactions of the pure solvents are given as insets: partial decomposition of DOL may lead to the formation of poly-DOL $(CH_2CH_2OCH_2)_n$, whereas the linear ether DME decomposes via deprotonation reactions to ethers and lithium alkoxides. Please note that the schematics are neither exhaustive nor true to scale.

magnitude higher for DME compared to DOL. Interestingly, the relative positions of maxima of S^- and $C_2H_2O^-$ signal intensities with respect to LiF^--maxima depend on the solvent: we assume that for DOL, sulfone species and alkoxides are dominant closer to the LE side of the SLEI than LiF. For DME these zones are reversed. Because of the broader and higher slope of $C_2H_2O^-$ in the SLEI formed in DME, we assume that a high fraction of alkoxide salts are formed in its deeper region. For a direct comparison, we refer to Figure S34 in the Supporting Information. In contrast, we assume that a higher fraction of LiOH is formed in the vicinity of the solid electrolyte in DOL, comparing the LiO^- fragments (which could either be attributed to SE fragments or the decomposition product LiOH) in Figure 5a,b. It may originate from SE surface degradation due to unavoidable water traces in the LE.[65] Via complementary analysis of reference material it can be shown that the CHO_2^- fragment assigned to formate and $CHO_{2,P}^-$, as a fragment of poly-DOL, are indeed distinguishable.[65] Compared to DME, we detect a significantly higher signal intensity for $CHO_{2,P}^-$ in the second region of the depth profile and assume that poly-DOL is a major constituent of the SLEI in DOL. DOL tends to decompose in a cationic process to polymeric species $(CH_2CH_2OCH_2O)_n$ catalyzed by Lewis acids[80,81] as denoted in **Figure 6**.

Based on these results, we propose an analogous solvent dependency of the SLEI composition as found for the SEI on lithium surfaces:[65] DOL initially creates an LiOH layer that is then covered by alkoxide salts, LiTFSI components, and LiF; DME forms an $R\text{-}CH_2OLi$ framework with embedded LiTFSI. The conducting salt decomposes subsequently, leading to massive LiF formation. As the SLEI in DME features significantly higher amounts of organic components like $C_2H_2O^-$ and CHO_2^-, we assume that DME has a higher tendency to decompose compared to DOL. A deprotonation of DME by Li^+ as depicted in Figure 6 may lead to its decomposition and additionally ease the formation of LiF out of protonated TFSI. For DOL, Aurbach et al. explained that the polymerization products, which are soluble ethers, interact with alkoxides, hydroxides, or oxides and partly dissolve them.[82] LiOH is not stable due to reaction with DOL and participates in the formation of soluble products.[82] Therefore, DOL has a lower tendency to form a chemically stable matrix, which would favor a highly resistive SLEI. In DME, a more rigid framework of alkoxides that is both more stable mechanically and chemically can incorporate LiTFSI, which successively decomposes to LiF that agglomerates to a dense film. Assuming that LiF is indeed a very poor ion conductor, which we extrapolate from the scarce literature values (10^{-9} S cm^{-1} at 50 °C)[83] to a range of (10^{-10} to 10^{-11}) S cm^{-1}, we explain the significant increase of the SLEI resistance in DME compared to DOL, as—exemplarily—a 1 nm thick layer will add at least 1000 Ω cm^2. Based on these discussions, we illustrate the local structures of the SLEIs formed in DOL- and DME-based electrolytes in Figure 6.

Finally, the depth profiles obtained for the binary electrolyte resemble a superposition of those found for the single solvents. We assume that both SLEI formation processes compete, leading to a more complex structure of the SLEI, as schematically denoted in Figure 6c. In the depth profiles, we define four different regions due to the intensity variations of the secondary ion signals. The profile for the lithium fluoride fragment LiF^- in the second region (red) is wider and more pronounced than for the DOL sample but substantially lower than for DME. Analogously to the SLEI in DOL, LiOH may form in the vicinity of the solid electrolyte, hinted at by the "bump" in the signal intensity of LiO^- in the third region (yellow). Alcoholate, carboxyle salt, and carbonate fragments present maxima in region III (yellow), whereas the signal intensity for $CHO_{2,P}^-$ assigned to $(CH_2CH_2OCH_2)_n$ (poly-DOL) are more pronounced at the beginning of sputtering (region I, blue and II, red). In contrast to the single solvent electrolytes, the signal intensity assigned to the LiTFSI fragment $NS_2O_4C_2F_6^-$ increases for longer sputter times (region III, yellow). By that, we assume that LiTFSI is covered by poly-DOL to some extent, which is supported by the XPS analysis presented above, showing comparably high intensities for the line attributed to poly-DOL and low intensities for the $-CF_3$ group assigned to LiTFSI. We propose that the accumulation of poly-DOL in the upper region of the SLEI may suppress the formation of a dense LiF layer—which may explain the lower resistance compared to the SLEI formed in pure DME unless it is thicker or more compact.

3. Conclusions

Within this study, we provide further evidence for the formation of solid/liquid electrolyte interphases (SLEIs) via in situ tracking

of the resistance contributions. The complementary analyses by means of EIS, XPS, and ToF-SIMS combined with depth profiling give rise to the following conclusions: i) in ethereal solvents DOL and DME, the SLEI grows on solid ion conductors LICGC ($R_{SLEI} \approx 70\ \Omega\ cm^2$) and LiPON ($R_{SLEI} \approx 600\ \Omega\ cm^2$ (C1) and $\approx 250\ \Omega\ cm^2$ (C2)) in an analogous way as previously presented for the model Li^+ solid electrolyte LAGP ($R_{SLEI} \approx 100\ \Omega\ cm^2$).[39,41,84] Similar findings for a combination of carbonaceous solvents and garnet-type solid electrolyte LLZTO ($R_{SLEI} \approx 600\ \Omega\ cm^2$)[57,58] give rise to the assumption that the phenomenon of the SLEI growth is indeed a general effect. ii) Comparing the magnitude of R_{SLEI} with the topologies of the LiPON samples with comparable chemical composition, a higher effective surface may indeed reduce the resistance contribution of the cell. Thus, as already assumed in our previous study,[41] tailoring the surface morphology to higher effective areas will reduce the SLEI resistance. However, considering that the very flat surface of LICGC does only lead to a mediocre R_{SLEI}, the chemical composition of the solid electrolyte surface is the more important factor to minimize polarization effects. iii) Finally, the liquid electrolyte solvents and the decomposition of LiTFSI govern the SLEI growth rate, composition, and resistance. This has been shown by comparing the SLEI effect in liquid electrolytes comprising DOL, DME, and the binary mixture DOL/DME. DME favors a fast increase in SLEI resistance which seems to proceed even after 165 h and surpasses 1000 $\Omega\ cm^2$. A dense LiF layer inside a stable carboxylate salt matrix is formed via decomposition of LiTFSI and DME. Meanwhile, DOL generates a SLEI mainly consisting of polymer species, which is slowly growing to a finite thickness, providing a lower resistance contribution $<100\ \Omega\ cm^2$. In the binary mixture of DOL and DME, both SLEI formation processes compete and the polymeric species tends to suppress LiF formation leading to a limited growth behavior. Based on this study, we propose the following next steps to gain further understanding on the SLEI phenomenon: sputter depth profiling may present a powerful tool to reveal the chemical composition of the interphase with adequate resolution, but thickness and density information is very scarce and hardly interpretable. Therefore, we propose to perform other methods, which are able to elucidate spatial dimensions of the SLEI. For example, analyses by in situ neutron reflectometry and quartz-crystal microbalance measurements, as already performed for LiPON in various LEs,[85] may also be applied for other SEs. While the SLEI adds a nonnegligible resistance contribution to hybrid electrochemical cells in many cases, it may also be used as protective layer. A NASICON-type SE, which is unstable against lithium metal, could be stabilized by addition of minuscule amounts of LE and the resulting SLEI formation.[43] Garnet-type LLZO employed in a Li–S cell enabled high cyclability by formation of a self-inhibiting SLEI containing polysulfide decomposition products.[46] In addition, *n*-butyllithium can also attenuate degradation of LLZO in contact with LE.[45] Thus, the applicability of other additives, which can hamper SLEI formation, should be explored. The vital role of transport across heterogeneous phase boundaries between solid and liquid ion conductors is not limited to protective coatings, hybrid cells, and hybrid electrolytes[84] but of core importance for all battery systems. We hope to motivate complementary experimental and theoretical studies to obtain further knowledge on the SLEI structure, its formation mechanisms, and its impact on ionic transport. Considering the variety of experimental data on that topic already acquired, we recently published a review on the existing data, as well studying the impact of the solid electrolyte, the solvent, and the conducting salt on the growth and magnitude of the SLEI's resistance.[86]

4. Experimental Section

Solid Electrolyte Preparation and Basic Analysis: LiPON thin films were sputtered on sapphire glass substrates for reference measurements and on porous alumina anodic oxidized (AAO) discs (13 mm diameter, 100 nm pores, Anodisc Inorganic Filter, Whatman plc, UK) for SLEI analysis. Radio-frequency magnetron sputtering (RF-MS) was carried out inside two different homemade reaction chambers, each under pure N_2 atmosphere. Chamber one (C1) was developed by SURFACE systems + technology, Germany, with an RF-MS system from Gencoa Ltd. placed below the samples and connected to a glovebox with Ar atmosphere (O_2 and H_2O below the detection limit of 1 ppm). Using transfer vessels, all samples created in this chamber could be post-processed without any contact to laboratory atmosphere. For morphology comparison and increased output, additional samples were created in a homemade chamber two (C2) with an RF-MS system by Gencoa Ltd. above the samples. As C2 was equipped with a loadlock system without glovebox, a short contact with lab atmosphere could not be omitted. In order to mitigate that influence, these samples were purged with Ar and sealed under Ar atmosphere immediately after deposition. Both systems made use of Li_3PO_4 targets (diameter 4 in (C1), 3 in (C2), Kurt J. Lesker Comp., USA) and a radio frequency of 13.56 MHz. The LiPON samples presented in this work were produced using the following parameter sets: (C1) RF power 200 W, bias: 50 V, N_2 partial pressure: 5×10^{-3} mbar; (C2) RF power: 100 W, bias: 0 V, N_2 partial pressure: 1.5×10^{-3} mbar. A sputter time of 450 min (120 min) in C1 (C2) led to a LiPON thickness of 4.5 µm (2.5 µm).

Lithium-ion conducting glass ceramic (LICGC) was purchased from Ohara GmbH, Germany as square plates with a thickness of 150 µm. These were cut into circular discs with a diameter of 12 mm, rinsed with dichloromethane and dried in a glass vacuum oven for 12 h at 170 °C (B.Ü.C.H.I., Switzerland) before postprocessing in gloveboxes (MBraun, Germany) under Ar atmosphere (O_2 and H_2O below the detection limit of 1 ppm).

Structural characterization of the glass-ceramic samples was performed by X-ray diffraction (XRD), using an Empyrean powder diffractometer (PANalytical, Netherlands) with Cu Kα radiation ($\lambda_1 = 154.056$ pm, $\lambda_2 = 154.539$ pm, $I(\lambda_2)/I(\lambda_1) = 0.5$ in Bragg–Brentano θ–θ geometry and a PIXcel^{3D} area detector with 255 measuring channels. Samples were pulverized, dispersed in ethanol, and placed on (911)-oriented silicon zero background holders. The program package FullProf Suite (version September 2018)[87] was used for structural refinements. Reflection profiles were fitted with a pseudo-Voigt function describing the peak profiles and a background by linear interpolation between manually set points with refinable heights. LiPON thermal stability was investigated up to a temperature of 500 °C inside an XRK 900 reaction chamber (Anton Paar, Austria) in flowing He atmosphere.

Topology information on the sample surface was obtained by means of AFM with a Nanosurf LensAFM and Easyscan 2 controller (Nanosurf AG, Switzerland) on a Halcyonics vibration isolating table (Accurion GmbH, Germany). LiPON samples were analyzed without further treatment and LICGC sample was rinsed with isopropyl alcohol and cleaned with a lint-free cloth. Data processing was performed with the Gwyddion software suite (version 2.51).[88]

The impedance behavior of the sole SEs was investigated by EIS, using different blocking electrode setups deposited via physical vapor deposition inside a home-made reaction chamber: for the LiPON thin films, two complementary electrode geometries were chosen: for lateral measurements, two rectangular electrodes were placed on top of the

LiPON thin-film as shown in Figure S6 (Supporting Information). For axial measurements, a line of Au electrodes was deposited on top of the substrate before LiPON deposition. After sputter deposition, a second line of Au was placed perpendicularly to the first one (Figure S8, Supporting Information). For the LICGC SE, Au films with a diameter of 10 mm were deposited on opposite sites. All EIS measurements were carried out using an Alpha-A high-performance frequency analyzer with a four-wire impedance test interface (Novocontrol, Germany). A perturbation amplitude of 10 mV and a frequency range of 20 MHz to 100 mHz was chosen. Impedance measurements with temperature variation were carried out in a thermostat/cryostat (Novocontrol, Germany) between –40 and 100 °C with a temperature accuracy of ±0.3 °C. In order to identify the electronic partial resistance, DC polarization measurements were performed using a homemade four-point setup with a Keithley sub-femto-Ampère source meter with preamplifier as voltage source and current meter and a Keithley 6517a high resistance meter for potential probing. A climatic chamber (Binder) and an additional faraday cage (Figure S10, Supporting Information) were used to suppress environmental effects. Herein, current was recorded for 24–72 h while applying DC potentials of 0.5–3.0 V.

Four-Point Impedance Spectroscopy Setup and Analysis (4P EIS): Proper identification and analysis of the resistance contribution of the solid/liquid electrolyte interphase (SLEI) was carried out with a homemade cell setup (Figure S15, Supporting Information) comprising two cylindrical compartments for the LE separated by the SE membrane. To ensure tightness of the setup, the cell body components were produced out of polyether ether ketone (PEEK) sealed with ethylene propylene diene monomer rubber (EPDM) gaskets. Prior to build-up, the brittle SE membranes were hot-sealed with polyethylene rings in a homemade hot press (Figure S16, Supporting Information) to inhibit LE by-pass. The electrode setup comprised two circular polished working electrodes and two point-like reference electrodes, all made of lithium metal (Chemetall GmbH, Germany) pressed into voids of the cell body. Lithium electrode contacting was performed via stainless steel feedthroughs, also sealed with EPDM gaskets. LE solutions of different concentrations of lithium bis(trifluoromethanesulfonyl)imide (LiTFSI, $LiN(SO_2CF_3)_2$, Ionic Liquid Technologies, Germany) were prepared: LiTFSI was dried at 170 °C for 24 h under vacuum inside a glass oven (B.Ü.C.H.I., Switzerland) and stored under Ar atmosphere. The solvents 1,3-dioxolane (DOL, $C_3H_6O_2$) and 1,2-dimethoxyethane (DME, $C_4H_{10}O_2$, both Sigma-Aldrich) were dried under reflux in Ar atmosphere inside a homemade Schlenk-line and stored over molecular sieve. By distillation process, the 75 ppm butylated hydroxytoluene (BHT) redox inhibitor was removed from DOL. Water content of all LEs used was below 5 ppm (by weight) determined by Karl–Fischer titration (831 KF coulometer, Metrohm, Germany). LiTFSI was weighed and dissolved into either the pure solvents or a 1:1 (v/v) mixture of the solvents by stirring longer than 48 h. LE solutions were simultaneously filled bubble-free into the two compartments (0.7 mL) to keep the geometry of the cylindrical cell setup with a cross-section of 1.13 cm^2 of every interface and avoid any mechanical strain on the membranes. Environmental conditions of the long-term measurements (up to 170 h) were stabilized using a Binder climatic chamber. For evaluation of the tightness and electrical correctness of the setup by means of complementary UV–vis and EIS analysis, the authors refer to the respective sections and Figures S17–S20 in the Supporting Information. All impedance data was analyzed using the RelaxIS 3 software (rhd Instruments, Germany) on the basis of a least-squares approximation. Additionally, the distribution of relaxation times (DRT) technique was used to obtain a deeper insight into the frequency evolution of the spectra. Using a homemade code based on the Python environment, impedance data was processed according to the assumptions and routines given in the Supporting Information.

Ex Situ Analysis: The SE samples analyzed in the four-point cell were rinsed three times with 100 µL of the respective solvent DOL, DME, or DOL/DME in the glovebox. One half was transferred into the XPS chamber, the other one into the ToF-SIMS chamber without any contact to lab atmosphere, using specially designed transfer vessels. XPS analysis was carried out with a Versaprobe II Scanning ESCA Microprobe device (Physical Electronics PHI, USA) using a monochromatized Al Kα X-ray source (1486.6 eV) with a spot size of 200 µm and an X-ray emission power of 50 W. Chamber pressure was in the range of 10^{-8} mbar and the electron energy analyzer was operated at a constant pass energy of 23.50 eV for XPS detail spectra, 93.9 eV for spectral acquisition during depth profiling, and 187.8 eV for survey spectra, respectively. In order to neutralize charging effects, the samples were flooded with low kinetic energy electrons and Ar^+ ions during data acquisition. Data analysis was performed using CasaXPS software package (Fairley, N. Casa XPS Version 2.3.17dev6.3a). Binding energies were referenced to the C 1s line with a binding energy of 284.8 eV. Detail spectra were modeled with mixed Gaussian–Lorentzian functions using a fixed FWHM for each element and a fixed area ratio of 2:1 for $2p_{3/2}$ and $2p_{1/2}$ lines. Depth profiles were obtained by Ar^+-ion sputtering on an area of (2×2) mm^2 with an acceleration voltage of 500 V and a current of 0.7 µA. Subsequent elemental quantification was done based on the RSFs provided by the instrument manufacturer.

ToF-SIMS sample analysis was performed with a ToF-SIMS^5 (ionToF, Germany) device equipped with a bismuth primary ion source (25 keV, (0.3 ± 0.06) pA) and a cesium sputter gun (500 eV, (40.7 ± 0.9) nA). In order to obtain profiles with high depth resolution and negligible crater wall effects, the analysis area of 91.1 µm² was centered in the sputter crater (450 µm²). The device was operated in negative ion mode to omit an incorrect representation of the signal intensity by detector saturation with Li^+. Data analysis was performed with SurfaceLab 6.5 software package (IonToF), normalizing the data by the total ion current in order to get rid of instrumental fluctuations and allow for comparison between the different samples. For comparability of the depth profiles, sputter times were referenced to the sputter current.

Supporting Information

Supporting Information is available from the Wiley Online Library or from the author.

Acknowledgements

The research presented herein was supported by the BASF Scientific Network for Electrochemistry and Batteries. The authors thank P. Hartmann and K. Leitner (BASF SE), B. Luerßen, B. Mogwitz, J. Sann, M. Elm, K. Michel, R. Oppermann, J. Neumeier, C. Barth, H. Weigand (Justus-Liebig-University Giessen), P. Adelhelm (University Jena), M. Falk (rhd Instruments), and H. W. Behm (Bosch Battery Systems Germany) for helpful discussions and scientific support. The authors appreciate fruitful discussions within the BASF SE Network for Electrochemistry and Batteries. Financial support by BMBF (Federal Ministry of Education and Research) within the project ELONGATE (03XP0248) is also acknowledged.

Conflict of Interest

The authors declare no conflict of interest.

Author Contributions

J.J. and M.R.B. conceived the experiments; M.R.B. designed the measurement setups and performed the electrochemical experiments with the assistance of T.D.; M.R.B., A.K., and M.G. performed the LiPON synthesis and analysis thereof with assistance of M.W.; K.O.H. developed the DRT algorithm and performed the DRT analysis; T.L., C.F., and M.R.B. carried out the XPS and ToF-SIMS experiments and evaluated the data; XRD measurements and Rietveld refinements were performed

by D.A.W. and M.R.B. The manuscript was written by M.R.B.; all the authors discussed the test results and commented on the manuscript.

Keywords

liquid electrolytes, post-lithium-ion batteries, SEI, solid electrolytes, solid electrolyte interphases

Received: March 2, 2020
Revised: June 25, 2020
Published online: August 18, 2020

[1] Z. Liu, W. Fu, C. Liang, in *Handbook of Battery Materials* (Eds: C. Daniel, J. O. Besenhard), Wiley-VCH Verlag GmbH & Co. KGaA, Weinheim, Germany **2012**, pp. 811–836.
[2] X. Ji, L. F. Nazar, *J. Mater. Chem.* **2010**, *20*, 9821.
[3] Y. V. Mikhaylik, J. R. Akridge, *J. Electrochem. Soc.* **2004**, *151*, A1969.
[4] B. L. Ellis, K. T. Lee, L. F. Nazar, *Chem. Mater.* **2010**, *22*, 691.
[5] M. R. Busche, P. Adelhelm, H. Sommer, H. Schneider, K. Leitner, J. Janek, *J. Power Sources* **2014**, *259*, 289.
[6] S.-E. Cheon, K.-S. Ko, J.-H. Cho, S.-W. Kim, E.-Y. Chin, H.-T. Kim, *J. Electrochem. Soc.* **2003**, *150*, A796.
[7] R. D. Rauh, K. M. Abraham, G. F. Pearson, J. K. Surprenant, S. B. Brummer, *J. Electrochem. Soc.* **1979**, *126*, 523.
[8] K. W. Leitner, H. Wolf, A. Garsuch, F. Chesneau, M. Schulz-Dobrick, *J. Power Sources* **2013**, *244*, 548.
[9] B. J. Bergner, A. Schürmann, K. Peppler, J. Janek, *J. Am. Chem. Soc.* **2014**, *136*, 15054.
[10] D. Aurbach, B. D. McCloskey, L. F. Nazar, P. G. Bruce, *Nat. Energy* **2016**, *1*, 16128.
[11] S. Xiong, K. Xie, Y. Diao, X. Hong, *J. Power Sources* **2014**, *246*, 840.
[12] Y. M. Lee, N.-S. Choi, J. H. Park, J.-K. Park, *J. Power Sources* **2003**, *119–121*, 964.
[13] A. C. Kozen, C. F. Lin, A. J. Pearse, M. A. Schroeder, X. Han, L. Hu, S. B. Lee, G. W. Rubloff, M. Noked, *ACS Nano* **2015**, *9*, 5884.
[14] G. Ma, Z. Wen, M. Wu, C. Shen, Q. Wang, J. Jin, X. Wu, *Chem. Commun.* **2014**, *50*, 14209.
[15] A. Manthiram, Y. Fu, S.-H. Chung, C. Zu, Y.-S. Su, *Chem. Rev.* **2014**, *114*, 11751.
[16] M. Barghamadi, A. Kapoor, C. Wen, *J. Electrochem. Soc.* **2013**, *160*, A1256.
[17] Y.-X. Yin, S. Xin, Y.-G. Guo, L.-J. Wan, *Angew. Chem., Int. Ed.* **2013**, *52*, 13186.
[18] L. Chen, L. L. Shaw, *J. Power Sources* **2014**, *267*, 770.
[19] S. S. Zhang, *J. Power Sources* **2013**, *231*, 153.
[20] J. Hassoun, B. Scrosati, *Angew. Chem., Int. Ed.* **2010**, *49*, 2371.
[21] X. Liang, Z. Wen, Y. Liu, H. Zhang, L. Huang, J. Jin, *J. Power Sources* **2011**, *196*, 3655.
[22] D. Marmorstein, T. H. Yu, K. A. Striebel, F. R. Mclarnon, J. Hou, E. J. Cairns, *J. Power Sources* **2000**, *89*, 219.
[23] J. Hassoun, B. Scrosati, *Adv. Mater.* **2010**, *22*, 5198.
[24] A. Hayashi, T. Ohtomo, F. Mizuno, K. Tadanaga, M. Tatsumisago, *Electrochem. Commun.* **2003**, *5*, 701.
[25] M. R. Busche, D. A. Weber, Y. Schneider, C. Dietrich, S. Wenzel, T. Leichtweiss, D. Schröder, W. Zhang, H. Weigand, D. Walter, S. J. Sedlmaier, D. Houtarde, L. F. Nazar, J. Janek, *Chem. Mater.* **2016**, *28*, 6152.
[26] Z. Jin, K. Xie, X. Hong, Z. Hu, X. Liu, *J. Power Sources* **2012**, *218*, 163.
[27] I. Bauer, S. Thieme, J. Brückner, H. Althues, S. Kaskel, *J. Power Sources* **2014**, *251*, 417.
[28] J. Q. Huang, Q. Zhang, H. J. Peng, X. Y. Liu, W. Z. Qian, F. Wei, *Energy Environ. Sci.* **2014**, *7*, 347.
[29] Z. Zhang, Y. Lai, Z. Zhang, K. Zhang, J. Li, *Electrochim. Acta* **2014**, *129*, 55.
[30] W. Li, J. Hicks-Garner, J. Wang, J. Liu, A. F. Gross, E. Sherman, J. Graetz, J. J. Vajo, P. Liu, *Chem. Mater.* **2014**, *26*, 3403.
[31] Q. Wang, J. Jin, X. Wu, G. Ma, J. Yang, Z. Wen, *Phys. Chem. Chem. Phys.* **2014**, *16*, 21225.
[32] A. Vizintin, M. U. M. Patel, B. Genorio, R. Dominko, *ChemElectroChem* **2014**, *1*, 1040.
[33] L. Wang, Y. Wang, Y. Xia, *Energy Environ. Sci.* **2015**, *8*, 1551.
[34] X. Yu, Z. Bi, F. Zhao, A. Manthiram, *ACS Appl. Mater. Interfaces* **2015**, *7*, 16625.
[35] X. Yu, Z. Bi, F. Zhao, A. Manthiram, *Adv. Energy Mater.* **2016**, *6*, 1601392.
[36] Q. Wang, Z. Wen, J. Jin, J. Guo, X. Huang, J. Yang, C. Chen, *Chem. Commun.* **2016**, *52*, 1637.
[37] R. Song, R. Fang, L. Wen, Y. Shi, S. Wang, F. Li, *J. Power Sources* **2016**, *301*, 179.
[38] Q. Wang, J. Guo, T. Wu, J. Jin, J. Yang, Z. Wen, *Solid State Ionics* **2017**, *300*, 67.
[39] H. Xu, S. Wang, A. Manthiram, *Adv. Energy Mater.* **2018**, *8*, 1800813.
[40] J.-Q. Huang, Q. Zhang, H.-J. Peng, X.-Y. Liu, W.-Z. Qian, F. Wei, *Energy Environ. Sci.* **2014**, *7*, 347.
[41] M. R. Busche, T. Drossel, T. Leichtweiss, D. A. Weber, M. Falk, M. Schneider, M. L. Reich, H. Sommer, P. Adelhelm, J. Janek, *Nat. Chem.* **2016**, *8*, 426.
[42] C. Wang, Y. Yang, X. Liu, H. Zhong, H. Xu, Z. Xu, H. Shao, F. Ding, *ACS Appl. Mater. Interfaces* **2017**, *9*, 13694.
[43] C. Wang, Q. Sun, Y. Liu, Y. Zhao, X. Li, X. Lin, M. N. Banis, M. Li, W. Li, K. R. Adair, D. Wang, J. Liang, R. Li, L. Zhang, R. Yang, S. Lu, X. Sun, *Nano Energy* **2018**, *48*, 35.
[44] B. J. Bergner, M. R. Busche, R. Pinedo, B. B. Berkes, D. Schröder, J. Janek, *ACS Appl. Mater. Interfaces* **2016**, *8*, 7756.
[45] B. Xu, H. Duan, H. Liu, C. Wang, S. Zhong, *ACS Appl. Mater. Interfaces* **2017**, *9*, 21077.
[46] K. "Kelvin" Fu, Y. Gong, S. Xu, Y. Zhu, Y. Li, J. Dai, C. Wang, B. Liu, G. Pastel, H. Xie, Y. Yao, Y. Mo, E. Wachsman, L. Hu, *Chem. Mater.* **2017**, *29*, 8037.
[47] Y. Seino, T. Ota, K. Takada, A. Hayashi, M. Tatsumisago, *Energy Environ. Sci.* **2014**, *7*, 627.
[48] S. Wenzel, D. A. Weber, T. Leichtweiss, M. R. Busche, J. Sann, J. Janek, *Solid State Ionics* **2016**, *286*, 24.
[49] F. Sagane, T. Abe, Y. Iriyama, Z. Ogumi, *J. Power Sources* **2005**, *146*, 749.
[50] T. Abe, M. Ohtsuka, F. Sagane, Y. Iriyama, Z. Ogumi, *J. Electrochem. Soc.* **2004**, *151*, A1950.
[51] F. Sagane, T. Abe, Z. Ogumi, *J. Phys. Chem. C* **2009**, *113*, 20135.
[52] I. Yamada, T. Abe, Y. Iriyama, Z. Ogumi, *Electrochem. Commun.* **2003**, *5*, 502.
[53] T. Abe, H. Fukuda, Y. Iriyama, Z. Ogumi, *J. Electrochem. Soc.* **2004**, *151*, A1120.
[54] Y. Yamada, F. Sagane, Y. Iriyama, T. Abe, Z. Ogumi, *J. Phys. Chem. C* **2009**, *113*, 14528.
[55] T. Abe, F. Sagane, M. Ohtsuka, Y. Iriyama, Z. Ogumi, *J. Electrochem. Soc.* **2005**, *152*, A2151.
[56] F. Sagane, T. Abe, Z. Ogumi, *J. Power Sources* **2010**, *195*, 7466.
[57] M. Schleutker, J. Bahner, C.-L. Tsai, D. Stolten, C. Korte, *Phys. Chem. Chem. Phys.* **2017**, *19*, 26596.
[58] J. Liu, X. Gao, G. O. Hartley, G. J. Rees, C. Gong, F. H. Richter, J. Janek, Y. Xia, A. W. Robertson, L. R. Johnson, P. G. Bruce, *Joule* **2020**, *4*, 101.
[59] B. Fleutot, B. Pecquenard, H. Martinez, M. Letellier, A. Levasseur, *Solid State Ionics* **2011**, *186*, 29.
[60] R. Marchand, D. Agliz, L. Boukbir, A. Quemerais, *J. Non-Cryst. Solids* **1988**, *103*, 35.
[61] V. Lacivita, A. S. Westover, A. K. Kercher, N. Phillip, G. Yang, G. M. Veith, G. Ceder, N. J. Dudney, *J. Am. Chem. Soc.* **2018**, *140*, 11029.
[62] J. B. Bates, N. J. Dudney, G. R. Gruzalski, R. A. Zuhr, A. Choudhury, C. F. Luck, J. D. Robertson, *Solid State Ionics* **1992**, *53–56*, 647.

[63] Y. Su, J. Falgenhauer, A. Polity, T. Leichtweiß, A. Kronenberger, J. Obel, S. Zhou, D. Schlettwein, J. Janek, B. K. Meyer, *Solid State Ionics* **2015**, *282*, 63.
[64] P. Hartmann, T. Leichtweiss, M. R. Busche, M. Schneider, M. Reich, J. Sann, P. Adelhelm, J. Janek, *J. Phys. Chem. C* **2013**, *117*, 21064.
[65] C. Fiedler, B. Luerssen, M. Rohnke, J. Sann, J. Janek, *J. Electrochem. Soc.* **2017**, *164*, A3742.
[66] R. Dedryvère, S. Leroy, H. Martinez, F. Blanchard, D. Lemordant, D. Gonbeau, *J. Phys. Chem. B* **2006**, *110*, 12986.
[67] S. Xiong, K. Xie, Y. Diao, X. Hong, *J. Power Sources* **2013**, *236*, 181.
[68] D. Ensling, M. Stjerndahl, A. Nytén, T. Gustafsson, J. O. Thomas, *J. Mater. Chem.* **2009**, *19*, 82.
[69] D. Aurbach, E. Pollak, R. Elazari, G. Salitra, C. S. Kelley, J. Affinito, *J. Electrochem. Soc.* **2009**, *156*, A694.
[70] H. Ota, Y. Sakata, Y. Otake, K. Shima, M. Ue, J. Yamaki, *J. Electrochem. Soc.* **2004**, *151*, A1778.
[71] Y. Hu, W. Kong, H. Li, X. Huang, L. Chen, *Electrochem. Commun.* **2004**, *6*, 126.
[72] A. Schechter, D. Aurbach, H. Cohen, *Langmuir* **1999**, *15*, 3334.
[73] D. Bar-Tow, E. Peled, L. Burstein, *J. Electrochem. Soc.* **1999**, *146*, 824.
[74] E. Peled, *J. Electrochem. Soc.* **1979**, *126*, 2047.
[75] D. Aurbach, A. Zaban, Y. Ein-Eli, I. Weissman, O. Chusid, B. Markovsky, M. Levi, E. Levi, A. Schechter, E. Granot, *J. Power Sources* **1997**, *68*, 91.
[76] B. Laik, A. Chaussé, R. Messina, M. G. Barthes-Labrousse, *Electrochim. Acta* **2001**, *46*, 691.
[77] K. Kanamura, H. Tamura, Z. Takehara, *J. Electroanal. Chem.* **1992**, *333*, 127.
[78] J. Vetter, P. Novák, M. R. Wagner, C. Veit, K. C. Möller, J. O. Besenhard, M. Winter, M. Wohlfahrt-Mehrens, C. Vogler, A. Hammouche, *J. Power Sources* **2005**, *147*, 269.
[79] A. M. Andersson, M. Herstedt, A. G. Bishop, K. Edström, *Electrochim. Acta* **2002**, *47*, 1885.
[80] G. H. Newman, R. W. Francis, L. H. Gaines, B. M. Rao, *J. Electrochem. Soc.* **1980**, *127*, 2025.
[81] P. G. Glugla, in *Proc. Electrochem. Soc.*, The Electrochemical Society, Schenectady, NY **1980**, pp. 407–416.
[82] D. Aurbach, O. Youngman, D. Pnina, *Electrochim. Acta* **1990**, *35*, 639.
[83] C. Li, L. Gu, J. Maier, *Adv. Funct. Mater.* **2012**, *22*, 1145.
[84] M. Keller, A. Varzi, S. Passerini, *J. Power Sources* **2018**, *392*, 206.
[85] M. Weiss, B.-K. Seidlhofer, M. Geiß, C. Geis, M. R. Busche, M. Becker, N. M. Vargas-Barbosa, L. Silvi, W. G. Zeier, D. Schröder, J. Janek, *ACS Appl. Mater. Interfaces* **2019**, *11*, 9539.
[86] M. Weiss, F. J. Simon, M. R. Busche, T. Nakamura, D. Schröder, F. H. Richter, J. Janek, *Electrochem. Energy Rev.* **2020**, *3*, 221.
[87] J. Rodríguez-Carvajal, *Phys. B* **1993**, *192*, 55.
[88] D. Nečas, P. Klapetek, *Open Phys.* **2012**, *10*, 181.